Chemical Science

ROYAL SOCIETY OF CHEMISTRY

EDGE ARTICLE

View Article Online
View Journal | View Issue

Cite this: *Chem. Sci.*, 2024, **15**, 12796

All publication charges for this article have been paid for by the Royal Society of Chemistry

Received 2nd June 2024
Accepted 8th July 2024

DOI: 10.1039/d4sc03612c

rsc.li/chemical-science

Efficient N_2 electroreduction enabled by linear charge transfer over atomically dispersed W sites†

Jin Wan,[a] Dong Liu,[a] Chuanzhen Feng,[a] Huijuan Zhang*[ab] and Yu Wang *[ab]

Electrocatalytic nitrogen reduction reaction (NRR) presents a sustainable alternative to the Haber–Bosch process for ammonia (NH_3) production. However, developing efficient catalysts for NRR and deeply elucidating their catalytic mechanism remain daunting challenges. Herein, we pioneered the successful embedding of atomically dispersed (single/dual) W atoms into $V_{2-x}CT_y$ *via* a self-capture method, and subsequently uncovered a quantifiable relationship between charge transfer and NRR performance. The prepared n-W/$V_{2-x}CT_y$ shows an exceptional NH_3 yield of 121.8 μg h^{-1} mg^{-1} and a high faradaic efficiency (FE) of 34.2% at −0.1 V (*versus* reversible hydrogen electrode (RHE)), creating a new record at this potential. Density functional theory (DFT) computations reveal that neighboring W atoms synergistically collaborate to significantly lower the energy barrier, achieving a remarkable limiting potential (U_L) of 0.32 V. Notably, the calculated U_L values for the constructed model show a well-defined linear relationship with integrated-crystal orbital Hamilton population (ICOHP) ($y = 0.0934x + 1.0007$, $R^2 = 0.9889$), providing a feasible activity descriptor. Furthermore, electronic property calculations suggest that the NRR activity is rooted in d–2π* coupling, which can be explained by the "donation and back-donation" hypothesis. This work not only designs efficient atomic catalysts for NRR, but also sheds new insights into the role of neighboring single atoms in improving reaction kinetics.

Introduction

Ammonia (NH_3) plays a vital role in our daily life, serving as a fundamental raw material for the manufacture of fertilizers, pharmaceuticals, and synthetic fibers.[1–3] Currently, the production of NH_3 heavily relies on the traditional Haber–Bosch process, which operates under harsh production conditions (300–500 °C and 200–300 atm), leading to high energy consumption and environmental pollution.[4,5] Thus, it is critical to explore sustainable and environmentally friendly approaches for NH_3 production. Electrocatalytic nitrogen (N_2) fixation demonstrates significant potential as an alternative to conventional processes, offering a straightforward method for converting N_2 to NH_3 in a mild environment.[6–8] Nevertheless, the electrocatalytic nitrogen reduction reaction (NRR, $N_2 + 6H^+ + 6e^- = 2NH_3$) suffers from sluggish kinetics due to the presence of inert N≡N bonds (bond energy = 941 kJ mol^{-1}), as well as the presence of competing hydrogen evolution reaction (HER) in the electrolyte, limiting the NH_3 yield and faradaic efficiency (FE).[9–11] To address the above challenges, the designed catalysts must exhibit high activity, selectivity and stability.

The emergence of atomically dispersed catalysts opens up opportunities for efficient NH_3 production due to their maximum atom utilization and outstanding catalytic properties.[12–14] Until now, numerous single atom catalysts (SACs), such as those incorporating Fe, Ru, Cu, Mo, and Mn atoms have been proven to be promising electrocatalysts for NH_3 production.[15–22] However, the simultaneous improvement of NH_3 yield and FE in the presence of multiple reaction intermediates remains a challenge for SACs. Furthermore, SACs with a single active site are rarely able to break the linear scaling relationship between the reaction intermediates.[10,23] By introducing another active site, dual atom catalysts (DACs) are equipped with more flexible active sites and interatomic synergies, thereby tuning the adsorption of intermediates and solving the drawbacks of SACs.[24–26] Recently, researchers mainly focus on various substrates, including carbon materials, carbon nitride compounds, and some organic porous materials, due to their abundance of available loading sites.[27–29] Unfortunately, the strong interactions between metal atoms may cause lattice distortions in these flexible substrates, resulting in poor stability. On the other hand, the presence of multiple reaction intermediates leads to unsatisfactory activity and complicates understanding of the reaction mechanism. Most of the studies emphasized that the catalytic activity originates from the electronic modulation between the dual atoms, but quantitative analysis of the relationship between charge transfer and activity remains ambiguous.[30,31] Thus, it is particularly crucial to

[a]*The School of Chemistry and Chemical Engineering, Chongqing University, 174 Shazheng Street, Shapingba District, Chongqing City, 400044, P. R. China*
[b]*College of Chemistry and Environmental Science, Inner Mongolia Normal University, Huhehaote, 010022, P. R. China. E-mail: zhanghj@cqu.edu.cn; wangy@cqu.edu.cn*

† Electronic supplementary information (ESI) available. See DOI: https://doi.org/10.1039/d4sc03612c

develop a robust conducting substrate for loading dual atoms to achieve efficient NRR activity and gain deep insights into NRR catalytic mechanism.

MXene, a cutting-edge two-dimensional material, holds immense potential for electrocatalytic applications. V_2CT_x MXene, a structural analog of $Ti_3C_2T_x$, can be synthesized by selectively etching V_2AlC MAX with hydrofluoric acid (HF). Boasting exceptional electrical conductivity and robust support for metal atom loading, V_2CT_x MXene, despite its current limited research, holds promising potential for significant advancements across a wide range of applications.[32–35] Due to the highly corrosive nature of HF, some V atoms adjacent to aluminum (Al) atoms are also etched away during the etching process, forming V single vacancies or vacancy clusters, providing opportunities for embedding foreign atoms.[36,37] These defects are inherently unstable and active, allowing metal atoms to be readily trapped under natural conditions after the addition of metal precursors.[38,39] Moreover, surface functional groups (T stands for –F, –O, and –OH) facilitate the electrosorption of metallic precursors, promoting the subsequent anchoring of metal atoms.[12,38] The embedded metal atoms in V vacancies generate strong C–metal bonds, sustaining the generation of various intermediates.

In view of these issues, we present a self-capture method for successfully synthesizing W atom-dispersed catalysts (defined as n-W/$V_{2-x}CT_y$, $n = 1, 2$) under mild conditions. The W atoms were successfully anchored into the V vacancies, forming stable W dual atom catalysts with a loading of ~1.39 wt%. The W atoms in n-W/V_2CT_x are surrounded by three C atoms, forming strong W–C bonds, as confirmed by aberration-corrected electron microscopy and synchrotron radiation characterization. Upon application to NRR, the prepared n-W/$V_{2-x}CT_y$ exhibited superior performance with NH_3 yield up to 121.8 $\mu g\ h^{-1}\ mg^{-1}$ and a FE of 34.2% at −0.1 V (*versus* reversible hydrogen electrode (RHE)). This performance surpasses the catalytic capabilities of $V_{2-x}CT_y$, WSAC/$V_{2-x}CT_y$, and W NPs/$V_{2-x}CT_y$, clearly indicating that the incorporation of neighboring W atoms in n-W/$V_{2-x}CT_y$ significantly boosted its NRR catalytic performance. Drawing from the experimental characterization results, three theoretical structural models were developed, including pure $V_{2-x}CT_y$, WSAC/$V_{2-x}CT_y$, and WDAC/$V_{2-x}CT_y$. Our density functional theory (DFT) calculations suggest that the incorporation of the neighboring active site significantly reduces the limiting potential (U_L) compared to pure $V_{2-x}CT_y$ and WSAC/$V_{2-x}CT_y$ (0.32, 0.81, and 0.71 V for WDAC/V_2CT_x, pure $V_{2-x}CT_y$, and WSAC/V_2CT_x, respectively). Furthermore, we constructed theoretical atomic models of W triple atom catalysts (WTAC/$V_{2-x}CT_y$) and W quadruple atom cluster catalysts (WQAC/$V_{2-x}CT_y$) to investigate the intrinsic relationship between charge transfer and NRR performance. Remarkably, these calculated U_L values exhibit a linear relationship with integrated-crystal orbital Hamilton population (ICOHP) ($y = 0.0934x + 1.0007$, $R^2 = 0.9889$). The synergistic interaction of W dual atoms can provide more d electrons to the $2\pi^*$ orbitals of N_2, intensifying the disruption of the N≡N bond and thus displaying outstanding NRR performance.

Results and discussion

As illustrated in Fig. 1a, multi-layer $V_{2-x}CT_y$ sheets were obtained by etching V_2AlC with HF solution. This process involves breaking the Al–V bonds and concurrent removal of some neighboring V atoms, ultimately leading to the formation of V single vacancies or vacancy clusters on the surface. The existence of V vacancy clusters allows dispersed W atoms to be embedded in adjacent vacancies, forming monatomic group structures. Subsequently, few-layer $V_{2-x}CT_y$ nanosheets were fabricated by stripping multi-layer $V_{2-x}CT_y$ sheets in tetrabutylammonium hydroxide (TBAOH) solution and then heat-treated to control the V surface primarily covered by O functional groups. Compared to –F and –OH groups, –O groups exhibit preferential adsorption of metal precursors, favoring the capture of single atoms.[40,41] Finally, WCl_6 powder was added to an aqueous solution containing $V_{2-x}CT_y$ with V vacancies. The unstable and reactive V vacancies efficiently capture free W ions, resulting in the formation of W atom-dispersed catalysts.

Scanning electron microscopy (SEM) images in Fig. S1 and S2† depict the changes in $V_{2-x}CT_y$ nanosheets before and after exfoliation. After etching V_2AlC MAX phases, the characteristic accordion-like structure of multi-layer $V_{2-x}CT_y$ is visible. Fig. S2† displays the distinct two-dimensional morphology of few-layer $V_{2-x}CT_y$, implying successful exfoliation of multi-layer $V_{2-x}CT_y$ nanosheets. Atomic force microscopy (AFM) images (Fig. S3†) suggest that the thickness of exfoliated $V_{2-x}CT_y$ nanosheets ranges from 4 to 6 nm. The high-angle annular dark-field scanning transmission electron microscopy (HAADF-STEM) and its energy-dispersive X-ray spectroscopy (EDS) elemental mapping in Fig. S4† demonstrate uniform distributions of elements (C, O, V), affirming the successful preparation of few-layer $V_{2-x}CT_y$ nanosheets. Additionally, V vacancies are vividly displayed by high-resolution TEM (HRTEM) in Fig. 1b and c. Selecting an area on the surface of $V_{2-x}CT_y$ and zooming in, we can clearly observe lattice fringes and some dark holes within the lattice, which are identified as V defects.

Upon the addition of the WCl_6 precursor, the X-ray diffraction (XRD) pattern of n-W/$V_{2-x}CT_y$ shows no significant difference from that of $V_{2-x}CT_y$, and no signals associated with crystalline W species are observed for n-W/$V_{2-x}CT_y$ (Fig. S5†). To examine the dispersion of W atoms and the surface morphology of n-W/$V_{2-x}CT_y$, aberration-corrected HAADF-STEM was applied. The results reveal uniform distribution of W atom pairs and isolated W atoms on the $V_{2-x}CT_y$ surface, accompanied by distinct lattice fringes (Fig. 1d and S6†). The intensity profiles confirm that the average spacing of neighboring W atoms is separated approximately 0.29 nm (Fig. 1e), confirming the homogeneous dispersion of the metal pairs and matching the theoretical structural modeling of the distance between W dual atoms (2.92 Å). Furthermore, the HAADF-STEM and EDS results demonstrate that the W atoms are evenly dispersed on the $V_{2-x}CT_y$ surface (Fig. 1g and h), without any detectable W nanoparticles, aligning with the XRD analysis. For comparative purposes, we modulated the concentration of HF, wherein a reduced HF concentration mitigates the disruption of the Al–V

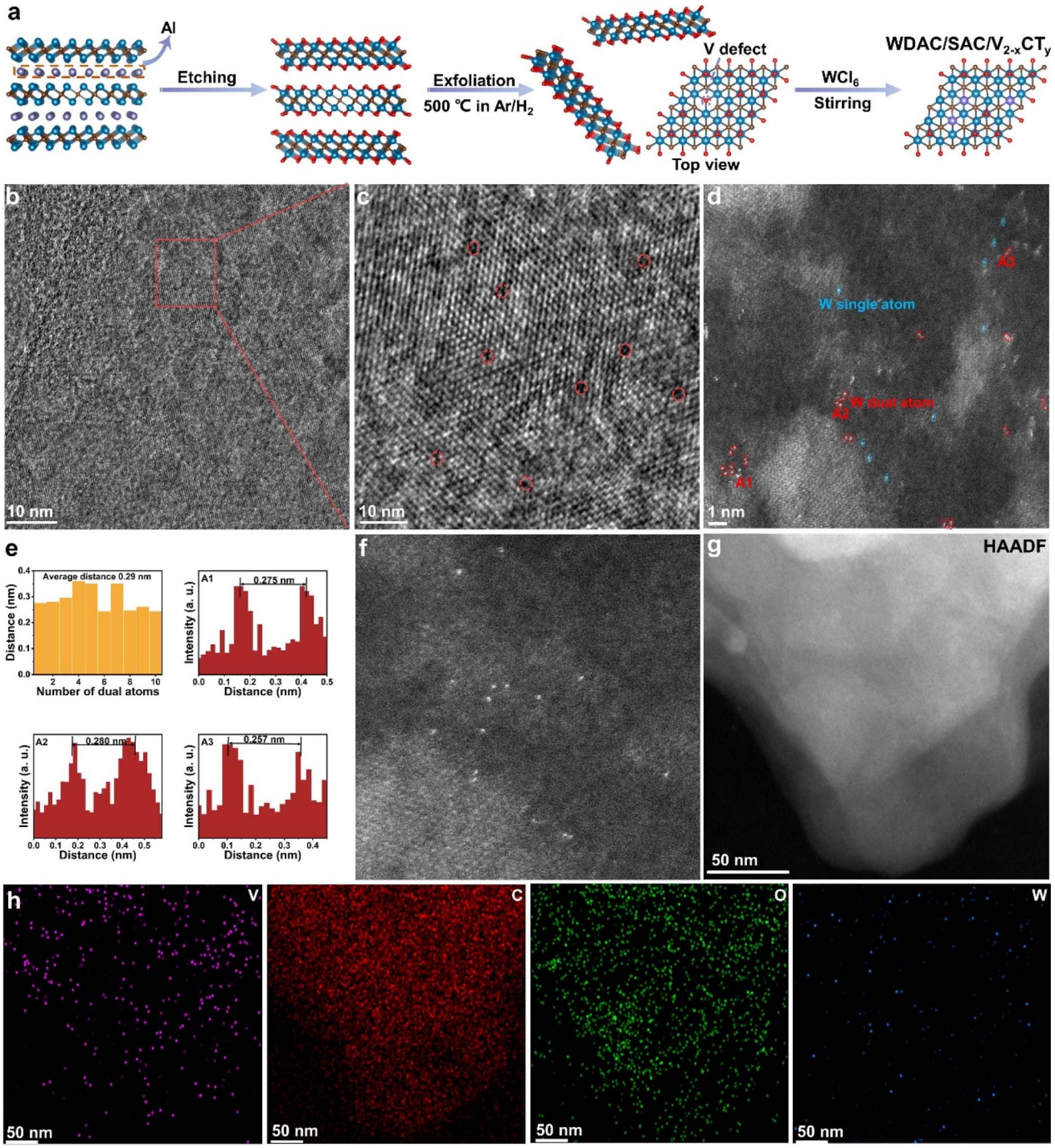

Fig. 1 (a) Schematic diagram of the synthesis of n-W/$V_{2-x}CT_y$. (b and c) HRTEM image of the $V_{2-x}CT_y$ layer and V vacancies on the $V_{2-x}CT_y$ surface. (d) Atomic-resolution HAADF-STEM image of atomically dispersed W atoms on the $V_{2-x}CT_y$ surface. (e) Intensity profiles obtained for WDAC/$V_{2-x}CT_y$. (f) Atomic-resolution HAADF-STEM image of single W atoms on the $V_{2-x}CT_y$ surface. (g and h) HAADF-STEM image and corresponding EDS mapping of n-W/$V_{2-x}CT_y$.

bonds. Consequently, this strategy lessens the formation of V vacancy clusters, ultimately leading to the majority of W atoms being securely embedded within single V vacancies. Fig. 1f and Fig. S7† present aberration-corrected HAADF-STEM and EDS images of WSAC/$V_{2-x}CT_y$, revealing a uniform distribution of isolated W atoms on the $V_{2-x}CT_y$ surface. Notably, the ICP-OES analysis (Table S1†) reveals that the W atomic content in n-W/$V_{2-x}CT_y$ stands at 1.39 wt%, whereas for WSAC/$V_{2-x}CT_y$, it is measured at 0.89 wt%. In addition, we prepared W nanoparticles loaded on the surface of $V_{2-x}CT_y$ (named W NPs/$V_{2-x}CT_y$) using a comparable approach by adding excess WCl_6 precursor. The ICP-OES results reveal that the W loading for W

NPs/$V_{2-x}CT_y$ is 5.12 wt%. HAADF-STEM clearly observes uniform arrangement of W nanoparticles on the $V_{2-x}CT_y$ surface, while EDS results indicate a higher content of W than n-W/$V_{2-x}CT_y$ (Fig. S8 and S9†).

To delve deeper into the atomic structure and coordination state of W atoms dispersed in n-W/$V_{2-x}CT_y$, we performed X-ray absorption near-edge structure (XANES), X-ray photoelectron spectroscopy (XPS), and extended X-ray absorption fine structure (EXAFS). Fig. 2a presents the XANES spectra of the W L3-edge relative to standard W foil, WO_3 and WC. The absorption threshold of n-W/$V_{2-x}CT_y$ is positioned between WC and WO_3, suggesting that the single W atom possessed a positive valence state (+4 to +6). The electronic structure and local coordination environment of W atoms were further analyzed using X-ray photoelectron spectroscopy (XPS) (Fig. S10†). The W 4f XPS spectrum of n-W/$V_{2-x}CT_y$ shows two peaks at 38.0 eV and 35.9 eV, corresponding to W $4f_{5/2}$ and W $4f_{7/2}$, respectively, corroborating the XANES results that the valence state of W atoms is near +6.[42] As shown in Fig. 2b, the EXAFS Fourier-transform (FT) curve of W in n-W/$V_{2-x}CT_y$ exhibits a prominent peak at 1.3 Å, assigned to the W–C bond.[43] An intense W–W characteristic peak at 2.6 Å in the W foil is absent in n-W/$V_{2-x}CT_y$, indicating the sole existence of atomically dispersed W in n-W/$V_{2-x}CT_y$. In addition, a wavelet transform (WT) was applied to W EXAFS, revealing the relationship between R and k space, as shown in Fig. 2d–f.[44,45] The WT EXAFS spectrum of n-W/$V_{2-x}CT_y$ displays an intensity maximum at ~7 $Å^{-1}$, correlating with the W–C bond. Unlike the W foil, no intensity contour is observed around 13 $Å^{-1}$, further validating the atomic dispersion of W atoms. To gain a profound understanding of the atomic structure and coordination state of W atoms, we performed EXAFS curve fitting. Our simulated EXAFS data, based on the WDAC/$V_{2-x}CT_y$ structure model, demonstrated a commendable alignment with the experimental findings. The fitted spectra expose the R space and k space of the n-W/$V_{2-x}CT_y$ system, which are presented in Fig. 2c and S11,† respectively. The inset of Fig. 2c offers a visual representation of the atomic structure model, highlighting the dual W atoms embedded within the $V_{2-x}CT_y$ lattice. Moreover, when we applied the same fitting procedure to the theoretical model of WSAC/$V_{2-x}CT_y$, the outcomes exhibited a similar trend to that of WDAC/$V_{2-x}CT_y$, attributed to their identical coordination environments (Fig. S12 and S13†). The EXAFS fittings disclose that the coordination number of isolated W atoms for n-W/$V_{2-x}CT_y$ is 3.6 ± 0.7, and the bond length is 1.97 ± 0.02 Å (Table S2†). This suggests that the W sites are primarily triply coordinated with C atoms.

The electrochemical NRR performance of n-W/$V_{2-x}CT_y$ was investigated under ambient conditions within an H-type electrolytic cell. The NH_3 yield and its by-product (hydrazine (N_2H_4)) were measured using a UV-vis spectrophotometer, and the corresponding calibration curves are shown in Fig. S14 and S15.† To begin, linear sweep voltammetry (LSV) was first conducted in N_2- and Ar-saturated 0.05 M H_2SO_4 electrolyte (Fig. 3a). The LSV curves reveal higher current density in N_2-saturated electrolyte compared to those in Ar-saturated between 0 and −0.7 V (*versus* RHE), suggesting that n-W/$V_{2-x}CT_y$ is active for the NRR. Subsequently, the NH_3 yields and corresponding FEs of n-W/$V_{2-x}CT_y$ were evaluated at various applied potentials by chronoamperometry tests (Fig. S16a†) and UV-Vis absorption spectroscopy (Fig. 3b and S17†). As shown in Fig. 3c, the NH_3 yield and FE reach the maximum values of 121.8 μg h^{-1} mg^{-1}

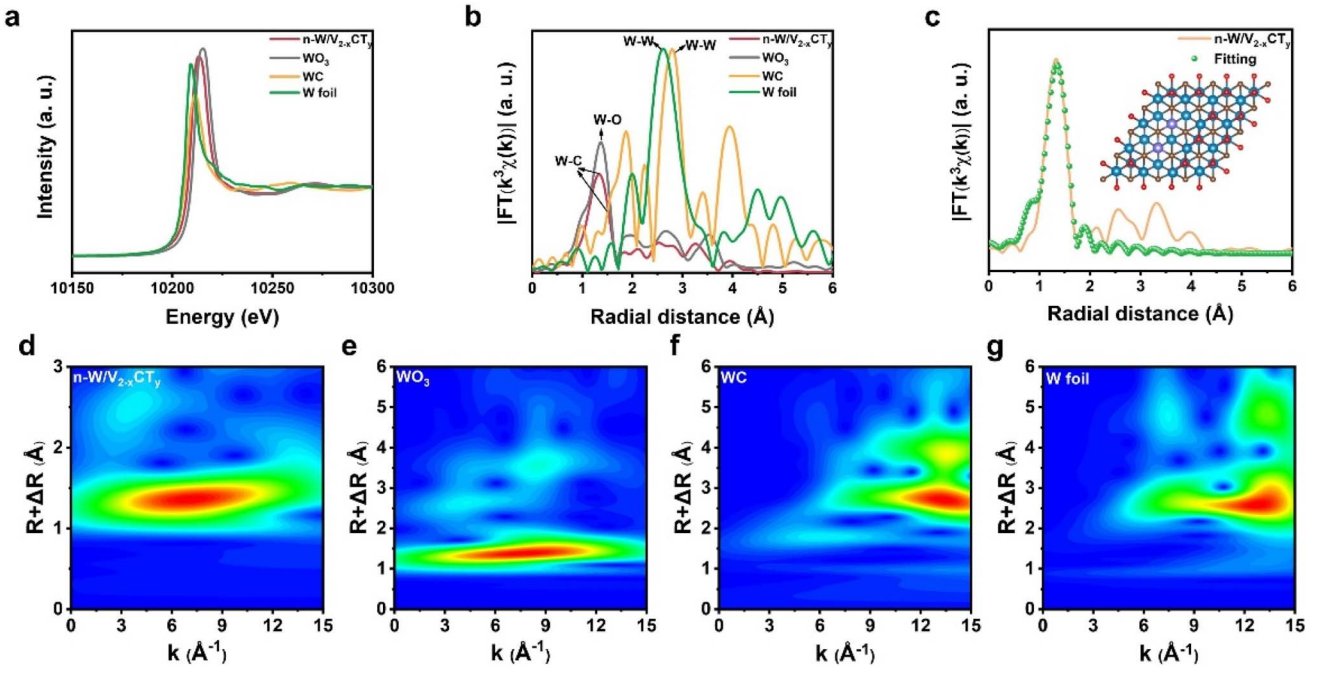

Fig. 2 (a) W K-edge XANES spectra of n-W/$V_{2-x}CT_y$, WO_3, WC, and W foil. (b) FT-EXAFS curves of n-W/$V_{2-x}CT_y$, WO_3, WC, and W foil. (c) FT-EXAFS fitting results of n-W/$V_{2-x}CT_y$ (inset: theoretical model of WDAC/$V_{2-x}CT_y$). (d–g) WT-EXAFS of n-W/$V_{2-x}CT_y$, WO_3, WC, and W foil, respectively.

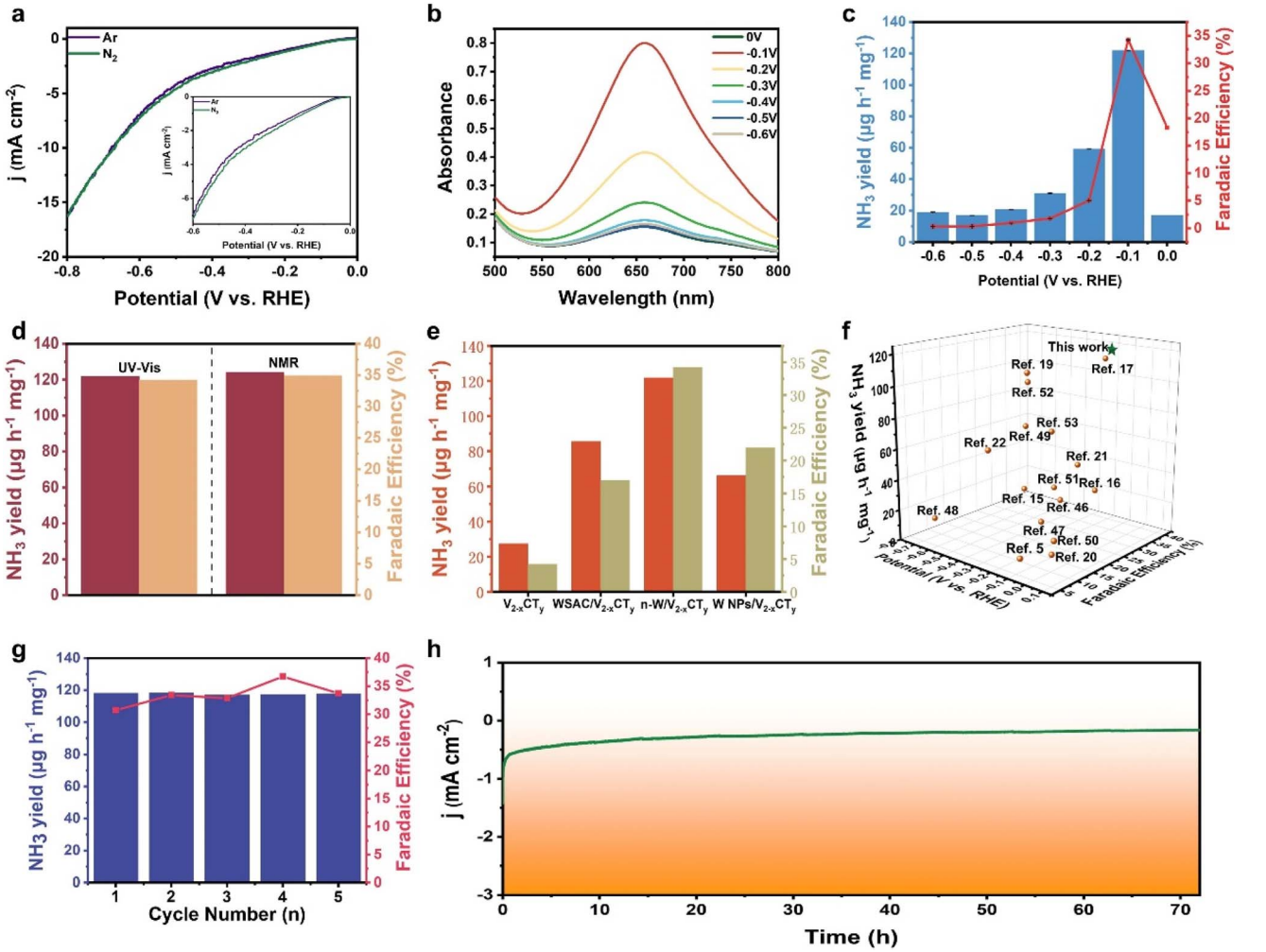

Fig. 3 (a) LSV curves in Ar- and N_2-saturated 0.05 M H_2SO_4 solution. (b) UV-Vis absorption spectra of the electrolytes at different potentials. (c) NH_3 yields and FEs at different applied potentials. (d) NH_3 yields and FEs measured on n-W/$V_{2-x}CT_y$ by NMR and UV-vis methods at −0.1 V (*versus* RHE). (e) NH_3 yields and FEs of $V_{2-x}CT_y$, WSAC/$V_{2-x}CT_y$, n-W/$V_{2-x}CT_y$, and W NPs/$V_{2-x}CT_y$ at −0.1 V (*versus* RHE). (f) Comparison of NH_3 yields and FEs of recently developed NRR electrocatalysts at respective potentials. (g) NH_3 yield and FE in cycle tests of n-W/$V_{2-x}CT_y$ at −0.1 V (*versus* RHE). (h) Chronoamperometric curve of n-W/$V_{2-x}CT_y$ during 72 h electrolysis.

and 34.2% at −0.1 V (*versus* RHE). It is noteworthy that as the applied potentials shift towards more negative values, there is a discernible decline in both the yield of NH_3 and its FE. This phenomenon is primarily attributed to the intensified competition between the HER and the desired reaction on the catalyst surface. Moreover, n-W/$V_{2-x}CT_y$ demonstrates exceptional selectivity for NH_3 production, as verified by the absence of detectable N_2H_4 (Fig. S16b†). To validate the accuracy of our detection method, we further quantified the NH_3 production using ^{1}H nuclear magnetic resonance (^{1}H NMR) analysis (Fig. S18†). The results showed that the NH_3 yield and FE of n-W/$V_{2-x}CT_y$ stood at 124.2 μg h^{-1} mg^{-1} and 34.9% at −0.1 V *versus* RHE, respectively. These results were in excellent agreement with those obtained through the indophenol blue method (Fig. 3d and S19†). We further tested NO_3^- concentration in the system (Fig. S20 and S21†). Based on the calibration curve, the calculated NO_3^- yield is 0.68 μg mL^{-1}, which is essentially negligible in the context of our experimental results. Since N-containing species (TBAOH) were utilized during the material synthesis, we conducted a test to evaluate the nitrogen reduction reaction (NRR) performance of n-W/$V_{2-x}CT_y$ at −0.1 V (*versus* RHE) under an Ar atmosphere. As depicted in Fig. S22,† the calculated NH_3 yields and FEs of n-W/$V_{2-x}CT_y$ were 4.2 μg h^{-1} mg^{-1} and 4.5%, respectively, implying negligible ammonia production.

To highlight the superior performance of the n-W/$V_{2-x}CT_y$ electrocatalyst, we examined the NRR activity of all comparative samples (including pure $V_{2-x}CT_y$ nanomeshes, WSAC/$V_{2-x}CT_y$, and W-NPs/$V_{2-x}CT_y$) across varying applied potentials. By analyzing the UV-Vis absorption spectra (Fig. S23–S28†), the optimal NH_3 yield and FE for each sample were determined and are presented in Fig. 3e. It can be concluded without doubt that the electrocatalyst of n-W/$V_{2-x}CT_y$ provides the highest NRR activity. This phenomenon clearly indicates that the incorporation of neighboring W atoms in n-W/$V_{2-x}CT_y$ significantly boosted its NRR catalytic performance. Moreover, we compared

the catalytic performance of n-W/$V_{2-x}CT_y$ with that of state-of-the-art NRR SACs (Fig. 3f and Table 1). n-W/$V_{2-x}CT_y$ possesses outstanding NRR performance at minimal potentials, presenting significant application potential. Besides high activity, an ideal NRR catalyst should be stable during the catalytic process, enabling sustained NH_3 production. We first investigated the NRR stability of n-W/$V_{2-x}CT_y$ by conducting consecutive electrolysis recycling and a 72 h long-term electrocatalytic test at a potential of −0.1 V (*versus* RHE). As shown in Fig. 3g and S29,† the NH_3 yield and FE of n-W/$V_{2-x}CT_y$ varied slightly over 5-cycle tests, demonstrating the excellent stability of n-W/$V_{2-x}CT_y$ toward NRR. The long-term electrocatalytic test result indicates a negligible decay in current density over 72 h, also suggesting good stability (Fig. 3h). In addition, the XRD and XPS analysis results of the n-W/$V_{2-x}CT_y$ electrocatalyst remained essentially unchanged before and after our stability test, further highlighting their structural stability (Fig. S30 and S31†). These results collectively reveal the superior stability of n-W/$V_{2-x}CT_y$ for NRR.

In order to validate the electrocatalytic activity of n-W/$V_{2-x}CT_y$ and decode the origin of its NRR performance, DFT calculations were performed to investigate the reaction mechanisms of NRR as well as the electronic properties of n-W/$V_{2-x}CT_y$ and $V_{2-x}CT_y$. Based on the experimental characterization results, we constructed theoretical structural models of pure $V_{2-x}CT_y$, WSAC/$V_{2-x}CT_y$, and WDAC/$V_{2-x}CT_y$. Under ambient conditions, N_2 molecules may adsorb on the catalyst either in side-on or end-on configurations. We first calculated the adsorption energy for different adsorption modes and the results are shown in Fig. 4a. The end-on configuration possesses a lower adsorption energy, which implies that the active site prefers to adsorb N_2 in an end-on configuration. According to the above results, we probed into the NRR route with an end-on configuration. Distal and alternative pathways were envisaged for the electrocatalytic conversion of N_2 to NH_3 (Fig. 4c and S32†). During the reaction sequences, the pre-reacted NN* can be transformed into NNH* by capturing a proton/electron (H^+/e^-) pair, a step that ordinarily serves as a potential-limiting step (PDS) due to the involvement of inert N≡N. The Gibbs free energy changes (ΔG) associated with this step on pure $V_{2-x}CT_y$ and WSAC/$V_{2-x}CT_y$ are 0.81 and 0.71 eV, respectively, and the initial hydrogenation procedure can occur spontaneously on WDAC/$V_{2-x}CT_y$ due to the presence of the doubly active site. Subsequently, the adsorbed NNH* intermediate can be hydrogenated into either NNH_2* or NHNH*. For the distal pathway, NNH_2* is further hydrogenated into the NNH_3* intermediate, and this step poses the greatest challenge for WDAC/$V_{2-x}CT_y$, featuring an energy barrier of 0.61 eV (Fig. S32†). In the ensuing stages, one NH_3 molecule is emitted, followed by the hydrogenation of the N* intermediate *via* the NH* → NH_2* → NH_3* sequence until the release of the second NH_3 molecule. By comparing the Gibbs free energy diagrams, it becomes apparent that WDAC/$V_{2-x}CT_y$ favors the alternative pathway, while the first hydrogenation step remains the most challenge for both pure $V_{2-x}CT_y$ and WSAC/$V_{2-x}CT_y$ (Fig. 4c). On the surface of WDAC/$V_{2-x}CT_y$, the NHNH* species proceeds through the NHNH* → $NHNH_2$* → NH_2NH_2* → 2NH_3* sequence, with the generation of NH_2NH_2* being identified as the PDS (0.32 eV). Briefly, we computed the limiting potential (U_L) value for these three catalysts, yielding U_L values of 0.81, 0.71, and 0.32 V for pure $V_{2-x}CT_y$, WSAC/$V_{2-x}CT_y$, and WDAC/$V_{2-x}CT_y$, respectively. As the theoretical simulation of reaction pathways relies solely on a vacuum model, we employed both implicit and explicit solvation models to investigate the PDS of the NRR process on WDAC/$V_{2-x}CT_y$, aiming to validate the credibility of our theoretical calculations. As detailed in Table S3,† all PDSs identified using the implicit solvation model exhibit exothermic characteristics. However, in the vacuum model, the hydrogenation step of $NHNH_2$* → NH_2NH_2* emerges as the determining PDS, possessing a limiting

Table 1 Performance comparison of reported electrocatalysts toward NRR

Catalyst	Electrolyte	Potential (V *vs.* RHE)	NH_3 yield (μg h^{-1} mg^{-1})	FE (%)	Ref
n-W/$V_{2-x}CT_y$	0.05 M H_2SO_4	−0.1	121.8	34.2	This work
Fe–S–C 700	0.1 M KOH	−0.1	8.8	6.1	5
Ru SAs/Ti_3C_2O	0.1 M HCl	−0.2	27.56	23.3	46
Fe_1S_x@TiO_2	0.1 M HCl	−0.2	18.3	17.3	47
SA-Ru@rGO/NC	0.1 M HCl	−0.3	110.1	17.9	19
W–NO/NC	0.5 M $LiClO_4$	−0.7	12.62	8.35	48
Mn–O_3N_1/PC	0.1 M HCl	−0.35	66.41	8.91	22
PdCu/NC	0.05 M H_2SO_4	−0.45	69.2	24.8	49
Mo_{SA}/CMF-S	0.1 M HCl	−0.2	46.6	28.9	21
$PdFe_1$	0.5 M $LiClO_4$	−0.2	111.9	37.8	17
Fe_{SA}-NSC-900	0.1 M HCl	−0.4	30.4	21.9	15
Ru SAs/g-C_3N_4	0.5 M NaOH	0.05	23	8.3	50
Zn/Fe–N–C	0.1 M PBS	−0.3	30.5	26.5	51
Fe-$(O–C_2)_4$	0.1 M KOH	−0.1	32.1	29.3	16
Fe–B/N–C	0.1 M HCl	−0.4	100.1	23	52
Cu SAs/TiO_2	0.5 M K_2SO_4	−0.05	6.26	12.88	20
Rh SA/GDY	0.005 M H_2SO_4, 0.1 M K_2SO_4, 0.01 M ascorbic acid	−0.2	74.15	20.36	53

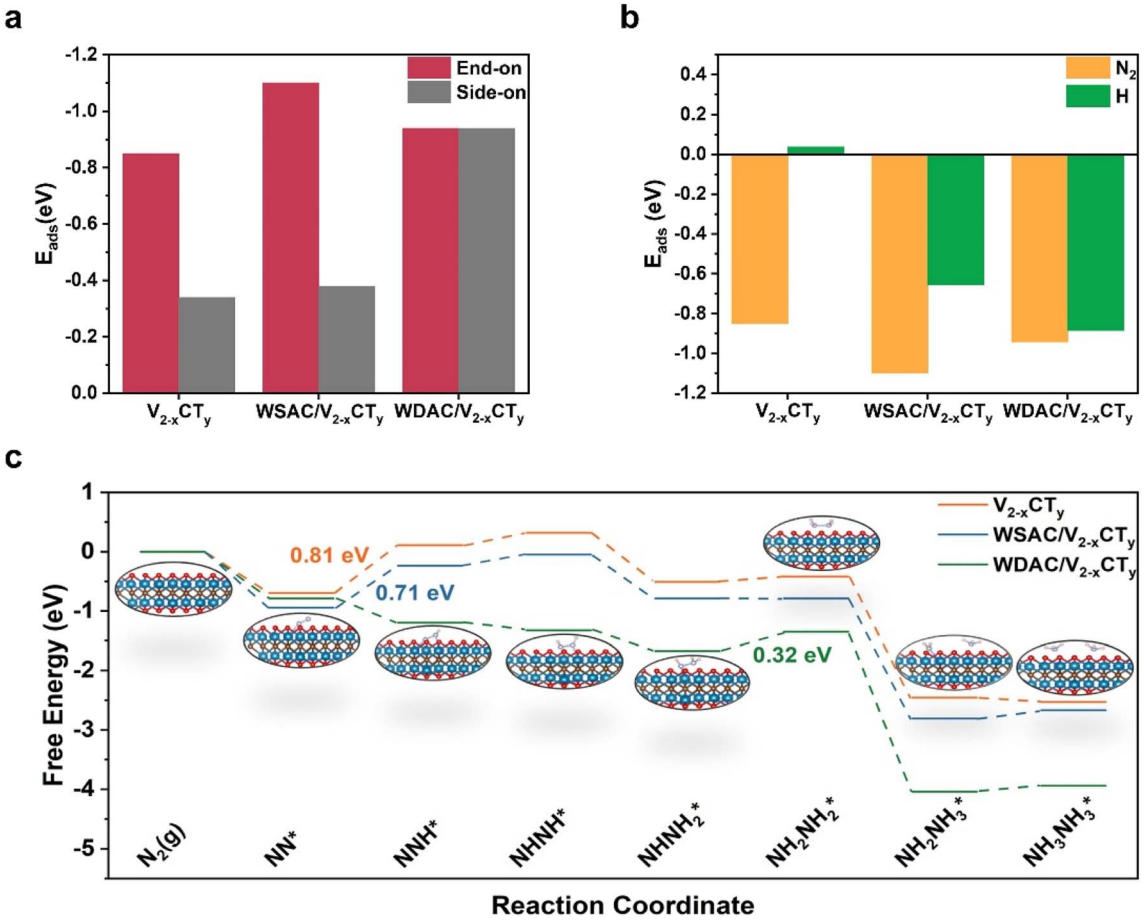

Fig. 4 (a) The adsorption energies of N_2 on $V_{2-x}CT_y$, $WSAC/V_{2-x}CT_y$, and $WDAC/V_{2-x}CT_y$ in side-on and end-on configurations, respectively. (b) The adsorption energies of $V_{2-x}CT_y$, $WSAC/V_{2-x}CT_y$, and $WDAC/V_{2-x}CT_y$ for N_2 and H, respectively. (c) Gibbs free energy diagrams of NRR *via* alternating pathways on $WDAC/V_{2-x}CT_y$, $WSAC/V_{2-x}CT_y$, and $V_{2-x}CT_y$, respectively.

potential of 0.32 V. To further validate the energy requirements of this critical step, we employed the explicit solvation model. As illustrated in Fig. S33,† the introduction of water molecules results in an energy requirement of 0.25 eV for the $NHNH_2$* → NH_2NH_2* step, which closely aligns with the limiting potential obtained from the vacuum model. This slight difference in overpotentials suggests that the theoretical calculations based on the vacuum model provide reliable insights into the reaction mechanism. The adsorption energies (E_{ads}) of N_2 and H on these three catalysts are presented in Fig. 4b. Considering the selectivity criterion, a catalyst with more negative E_{ads} suggests a greater preference for the corresponding pre-processed reaction, thereby offering improved selectivity. Surprising, all three systems show more negative E_{ads} for N_2.

We delved deeper into understanding the origin of the active site's electrocatalytic behavior by examining the charge density difference, partial density of states (PDOS), and integrated-crystal orbital Hamilton population (ICOHP). As illustrated in Fig. 5b and S37,† N_2 molecules adsorbed on the active sites in an end-on configuration with substantial electron transfer. The adsorbed N_2 can interact with the active sites through the so-called "donation and back-donation" process, where the active sites can donate electrons into the antibonding orbitals of N_2, while N_2 donates electrons back to the d orbitals of metal atoms. Bader charge calculations were employed to quantify the relationship between the extent of charge transfer and the elongation N≡N bond. Particularly, the W atoms of WDAC/$V_{2-x}CT_y$ contribute more electrons to the antibonding orbitals of N_2 compared to $WSAC/V_{2-x}CT_y$ and $V_{2-x}CT_y$, causing a noticeable elongation of the N_2 bond (1.20 Å *vs.* 1.12 Å for free N_2). Importantly, $WSAC/V_{2-x}CT_y$ can offer more electrons to N_2 than pure $V_{2-x}CT_y$, and the introduction of another W atom augments the electron donor for N_2 (0.169 e^-, 0.187 e^-, and 0.732 e^- for $V_{2-x}CT_y$, $WSAC/V_{2-x}CT_y$, and $WDAC/V_{2-x}CT_y$, respectively). More electrons are supplied to the antibonding orbitals of N_2, promoting the activation of N_2. The PDOS of free N_2 and these three systems is displayed in Fig. S38 and S39.† Referring to the molecular orbitals of free N_2, as N_2 adsorbed onto the active site, the d orbitals of W atoms push electrons to the antibonding orbitals of N_2, causing a negative shift of the partially occupied $2\pi^*$ orbital close to the Fermi level. The ICOHP results further illustrate the activation of N_2 on the active site (Fig. 5a). The computed ICOHP for $WDAC/V_{2-x}CT_y$ is more negative than those for $WSAC/V_{2-x}CT_y$ and pure $V_{2-x}CT_y$,

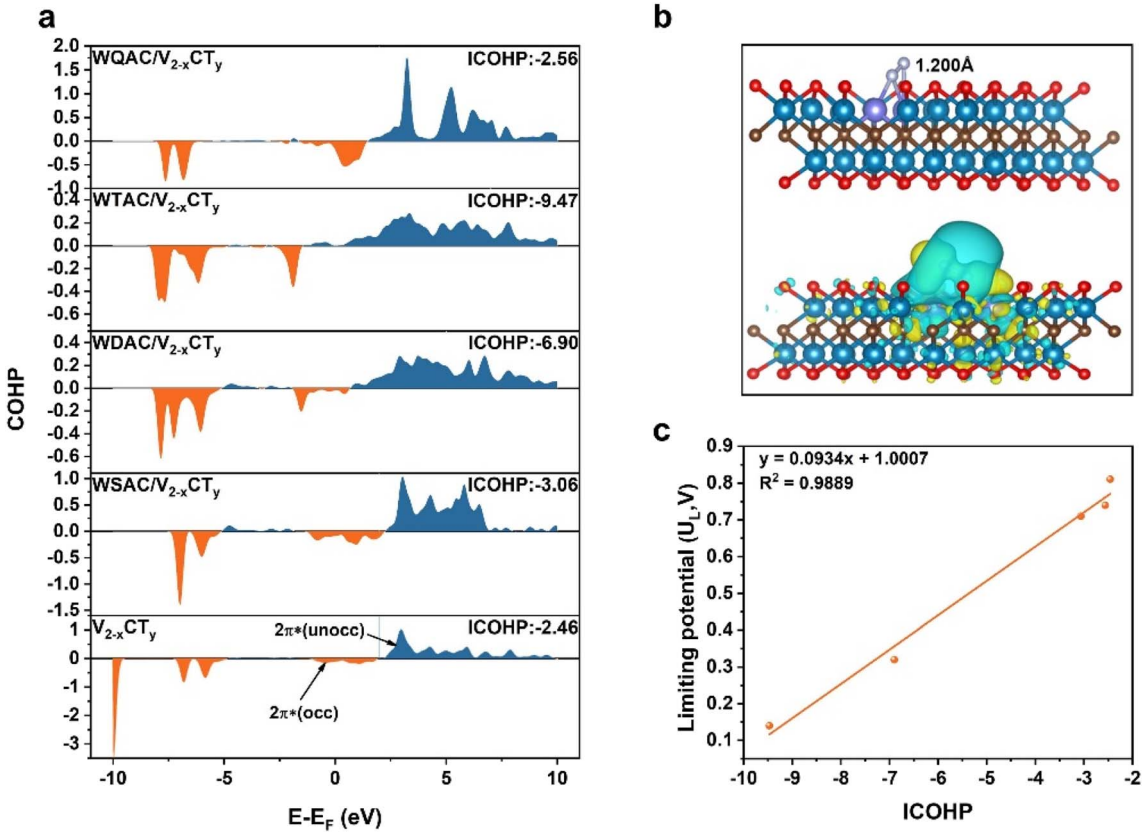

Fig. 5 (a) The COHPs of N_2 on $V_{2-x}CT_y$, WSAC/$V_{2-x}CT_y$, WDAC/$V_{2-x}CT_y$, WTAC/$V_{2-x}CT_y$, and WQAC/$V_{2-x}CT_y$ surfaces (orange and blue denote bonding and antibonding states, respectively). (b) Optimized structures and charge density differences of N_2 on the WDAC/$V_{2-x}CT_y$ surface (cyan and yellow represent charge depletion and accumulation, respectively. The isosurface value is 0.001 e Å^{-3}). (c) The line relationship between ICOHP and limiting potential.

suggesting that the interaction between N and W is more robust in WDAC/$V_{2-x}CT_y$, leading to superior activation of N_2 on the WDAC/$V_{2-x}CT_y$ surface.

To quantify the relationship between the charge transfer and NRR performance. We further constructed theoretical atomic models of W triple atom catalysts (WTAC/$V_{2-x}CT_y$) and W quadruple atom cluster catalysts (WQAC/$V_{2-x}CT_y$) for comparison. The adsorption and activation of N_2 on the surfaces of WTAC/$V_{2-x}CT_y$ and WQAC/$V_{2-x}CT_y$ were first examined. The results show that N_2 also tends to adsorb on these two catalyst surfaces in an end-on configuration, and the calculated U_L values for WTAC/$V_{2-x}CT_y$ and WQAC/$V_{2-x}CT_y$ are 0.14 and 0.74 V, respectively (Fig. S34S36†). Electronic property calculations show that WTAC/$V_{2-x}CT_y$ and WQAC/$V_{2-x}CT_y$ also follow the rule that strong d–2π* coupling leads to higher NRR activity (Fig. S37 and S39†). By correlating the ICOHP values with the calculated U_L values, the results reveal a strong linear relationship between the two ($y = 0.0934x + 1.0007$, $R^2 = 0.9889$), providing a practical descriptor for predicting the NRR performance (Fig. 5c).

Conclusions

In summary, n-W/$V_{2-x}CT_y$ was rationally synthesized by a self-capture approach. HAADF-STEM and EXAFS results revealed that W single/dual atoms were successfully embedded in V single vacancies or vacancy clusters, forming stable W–C bonds with three neighboring C atoms. A notable NH_3 yield of 121.8 μg h^{-1} mg^{-1} and a substantial FE of 34.2% at −0.1 V (*versus* RHE) were achieved, establishing a new record at this potential level. This exceptional performance exceeds the catalytic capabilities of $V_{2-x}CT_y$, WSAC/$V_{2-x}CT_y$, and W NPs/$V_{2-x}CT_y$, unequivocally demonstrating that the integration of neighboring W atoms in n-W/$V_{2-x}CT_y$ substantially enhances its NRR catalytic performance. Moreover, the exceptional stability of n-W/$V_{2-x}CT_y$ with a negligible decay of current density over 72 h primarily stems from the robust W–C bond. DFT calculations demonstrated that the additional W atom contributes to the improvement of the reactivity of WDAC/$V_{2-x}CT_y$ by donating more d electrons to the 2π* orbitals of N_2. This donation results in the better activation of the inert N≡N bonds and lowering of the reaction energy barrier (the calculated U_L values for pure $V_{2-x}CT_y$, WSAC/$V_{2-x}CT_y$, and WDAC/$V_{2-x}CT_y$ are 0.81, 0.71, and 0.32 V, respectively). Furthermore, a quantitative investigation of the correlation between the calculated U_L and the amount of charge transfer was conducted. The results indicated that there exists a well-defined linear relationship between the calculated U_L and ICOHP values ($y = 0.0934x + 1.0007$, $R^2 = 0.9889$). Our finding opens up new avenues for the design of higher activity atomic

catalysts and provides novel insights into understanding the catalytic mechanism of NRR.

Data availability

The data that support the findings of this study are available from the corresponding authors upon reasonable request.

Author contributions

Y. W. conceived and supervised the research; J. W. and C. Z. F. synthesized the catalysts and performed the catalysis experiments; J. W. performed DFT calculations; D. L. and H. J. Z. provided experimental measurements and STEM images; Y. W., C. Z. F., H. J. Z. and J. W. analyzed the data and wrote the paper; Y. W. discussed the results and commented on the manuscript.

Conflicts of interest

The authors declare no competing interests.

Acknowledgements

This work was financially supported by the Fundamental Research Funds for the Central Universities (0301005202017, 2018CDQYFXCS0017, and 106112017CDJXSYY0001), Thousand Young Talents Program of the Chinese Central Government (Grant No. 0220002102003), National Natural Science Foundation of China (NSFC, Grant No. 22371022, 22271029, U19A20100, 21971027, 21373280, and 21403019), Beijing National Laboratory for Molecular Sciences (BNLMS) and Hundred Talents Program at Chongqing University (Grant No. 0903005203205), The State Key Laboratory of Mechanical Transmissions Project (SKLMT-ZZKT-2017M11), Natural Science Foundation of Chongqing (Grant No. cstc2019jcyj-msxmX0426), and Science and Technology Research Project of Education Agency in Chongqing (Grant No. KJZDK201800102).

References

1 J. G. Chen, R. M. Crooks, L. C. Seefeldt, K. L. Bren, R. M. Bullock, M. Y. Darensbourg, P. L. Holland, B. Hoffman, M. J. Janik, A. K. Jones, M. G. Kanatzidis, P. King, K. M. Lancaster, S. V. Lymar, P. Pfromm and W. F. Schneider, *Science*, 2018, **360**, eaar6611.
2 L. Wang, M. Xia, H. Wang, K. Huang, C. Qian, C. T. Maravelias and G. A. Ozin, *Joule*, 2018, **2**, 1055–1074.
3 B. C. Cui, S. Licht, B. Wang, F.-F. Li, J. Lau and S. Liu, *Science*, 2014, **345**, 637–640.
4 J. W. Erisman, M. A. Sutton, J. Galloway, Z. Klimont and W. Winiwarter, *Nat. Geosci.*, 2008, **1**, 636–639.
5 M. I. Ahmed, L. J. Arachchige, Z. Su, D. B. Hibbert, C. Sun and C. Zhao, *ACS Catal.*, 2022, **12**, 1443–1451.
6 Z. W. Seh, J. Kibsgaard, C. F. Dickens, I. B. Chorkendorff, J. K. Norskov and T. F. Jaramillo, *Science*, 2017, **355**, 146.
7 G. Soloveichik, *Nat. Catal.*, 2019, **2**, 377–380.
8 H. S. Kim, J. Choi, J. Kong, H. Kim, S. J. Yoo and H. S. Park, *ACS Catal.*, 2020, **11**, 435–445.
9 J. Wan, Y. Wang, W. Tian, H. Zhang and Y. Wang, *Appl. Surf. Sci.*, 2021, **569**, 151020.
10 X. Guo, J. Gu, S. Lin, S. Zhang, Z. Chen and S. Huang, *J. Am. Chem. Soc.*, 2020, **142**, 5709–5721.
11 M. Li, Y. Cui, X. Zhang, Y. Luo, Y. Dai and Y. Huang, *J. Phys. Chem. Lett.*, 2020, **11**, 8128–8137.
12 J. Zhang, Y. Zhao, X. Guo, C. Chen, C.-L. Dong, R.-S. Liu, C.-P. Han, Y. Li, Y. Gogotsi and G. Wang, *Nat. Catal.*, 2018, **1**, 985–992.
13 B. Qiao, A. Wang, X. Yang, L. F. Allard, Z. Jiang, Y. Cui, J. Liu, J. Li and T. Zhang, *Nat. Chem.*, 2011, **3**, 634–641.
14 J. Li, M. F. Stephanopoulos and Y. Xia, *Chem. Rev.*, 2020, **120**, 11699–11702.
15 Y. Li, Y. Ji, Y. Zhao, J. Chen, S. Zheng, X. Sang, B. Yang, Z. Li, L. Lei, Z. Wen, X. Feng and Y. Hou, *Adv. Mater.*, 2022, **34**, e2202240.
16 S. Zhang, M. Jin, T. Shi, M. Han, Q. Sun, Y. Lin, Z. Ding, L. R. Zheng, G. Wang, Y. Zhang, H. Zhang and H. Zhao, *Angew Chem. Int. Ed. Engl.*, 2020, **59**, 13423–13429.
17 X. Li, P. Shen, Y. Luo, Y. Li, Y. Guo, H. Zhang and K. Chu, *Angew Chem. Int. Ed. Engl.*, 2022, **61**, e202205923.
18 H. C. Tao, C. Choi, L. X. Ding, Z. Jiang, Z. S. Hang, M. W. Jia, Q. Fan, Y. N. Gao, H. H. Wang, A. W. Robertson, S. Hong, Y. S. Jung, S. Z. Liu and Z. Y. Sun, *Chem*, 2019, **5**, 204–214.
19 Y. Chen, R. Xu, Y. Li, L. Cai, Y. Yang, Y. Zheng, C. Zuo, H. Huang, Z. Wen and Q. Wang, *Chem. Commun.*, 2023, **59**, 5403–5406.
20 Z. Q. Zhao, K. Li, J. Liu, J. J. Mao and Y. Q. Lin, *Small*, 2023, **19**, e2206626.
21 L. Li, W. Yu, W. Gong, H. Wang, C.-L. Chiang, Y. Lin, J. Zhao, L. Zhang, J.-M. Lee and G. Zou, *Appl. Catal., B*, 2023, **321**, 122038.
22 L. Han, M. Hou, P. Ou, H. Cheng, Z. Ren, Z. Liang, J. A. Boscoboinik, A. Hunt, I. Waluyo, S. Zhang, L. Zhuo, J. Song, X. Liu, J. Luo and H. L. Xin, *ACS Catal.*, 2020, **11**, 509–516.
23 Z. W. Chen, J.-M. Yan and Q. Jiang, *Small Methods*, 2019, **3**, 1800291.
24 W. H. Li, J. Yang and D. Wang, *Angew Chem. Int. Ed. Engl.*, 2022, **61**, e202213318.
25 A. Pedersen, J. Barrio, A. Li, R. Jervis, D. J. L. Brett, M. M. Titirici and I. E. L. Stephens, *Adv. Energy Mater.*, 2021, **12**, 2102715.
26 L. J. Arachchige, Y. Xu, Z. Dai, X. Zhang, F. Wang and C. Sun, *J. Phys. Chem. C*, 2020, **124**, 15295–15301.
27 M. Zhang, Z. Hu, L. Gu, Q. Zhang, L. Zhang, Q. Song, W. Zhou and S. Hu, *Nano Res.*, 2020, **13**, 3206–3211.
28 P. Peljo, L. Murtomaki, T. Kallio, H. J. Xu, M. Meyer, C. P. Gros, J. M. Barbe, H. H. Girault, K. Laasonen and K. Kontturi, *J. Am. Chem. Soc.*, 2012, **134**, 5974–5984.
29 Y. Zhang, J. Hu, C. Zhang, Y. Liu, M. Xu, Y. Xue, L. Liu and M. K. H. Leung, *J. Mater. Chem. A*, 2020, **8**, 9091–9098.
30 Y. N. Gong, C. Y. Cao, W. J. Shi, J. H. Zhang, J. H. Deng, T. B. Lu and D. C. Zhong, *Angew Chem. Int. Ed. Engl.*, 2022, **61**, e202215187.

31 W. Zhao, C. Luo, Y. Lin, G.-B. Wang, H. M. Chen, P. Kuang and J. Yu, *ACS Catal.*, 2022, **12**, 5540–5548.
32 J. Wan, Y. Wang, H. Zhang and Y. Wang, *Chem. Eng. J.*, 2023, **470**, 144151.
33 E. Ghasali, Y. Orooji, A. Azarniya, M. Alizadeh, M. Kazem-zad and T. Ebadzadeh, *Appl. Surf. Sci.*, 2021, **542**, 148538.
34 F. Liu, J. Zhou, S. Wang, B. Wang, C. Shen, L. Wang, Q. Hu, Q. Huang and A. Zhou, *J. Electrochem. Soc.*, 2017, **164**, A709–A713.
35 A. VahidMohammadi, A. Hadjikhani, S. Shahbazmohamadi and M. Beidaghi, *ACS Nano*, 2017, **11**, 11135–11144.
36 S. Zhou, Y. Zhao, R. Shi, Y. Wang, A. Ashok, F. Heraly, T. Zhang and J. Yuan, *Adv. Mater.*, 2022, **34**, e2204388.
37 D. Zhao, Z. Chen, W. Yang, S. Liu, X. Zhang, Y. Yu, W.-C. Cheong, L. Zheng, F. Ren, G. Ying, X. Cao, D. Wang, Q. Peng, G. Wang and C. Chen, *J. Am. Chem. Soc.*, 2019, **141**, 4086–4093.
38 Z. Li, Y. Cui, Z. Wu, C. Milligan, L. Zhou, G. Mitchell, B. Xu, E. Shi, J. T. Miller, F. H. Ribeiro and Y. Wu, *Nat. Catal.*, 2018, **1**, 349–355.
39 Z. Zhang, H. Li, G. Zou, C. Fernandez, B. Liu, Q. Zhang, J. Hu and Q. Peng, *ACS Sustainable Chem. Eng.*, 2016, **4**, 6763–6771.
40 Z. Fu, N. Wang, D. Legut, C. Si, Q. Zhang, S. Du, T. C. Germann, J. S. Francisco and R. Zhang, *Chem. Rev.*, 2019, **119**, 11980–12031.
41 I. Persson, J. Halim, T. W. Hansen, J. B. Wagner, V. Darakchieva, J. Palisaitis, J. Rosen and P. O. Å. Persson, *Adv. Funct. Mater.*, 2020, **30**, 1909005.
42 J. Yan, L. Kong, Y. Ji, J. White, Y. Li, J. Zhang, P. An, S. Liu, S. T. Lee and T. Ma, *Nat. Commun.*, 2019, **10**, 2149.
43 W. Chen, J. Pei, C. T. He, J. Wan, H. Ren, Y. Wang, J. Dong, K. Wu, W. C. Cheong, J. Mao, X. Zheng, W. Yan, Z. Zhuang, C. Chen, Q. Peng, D. Wang and Y. Li, *Adv. Mater.*, 2018, **30**, e1800396.
44 H. Funke, A. C. Scheinost and M. Chukalina, *Phys. Rev. B*, 2005, **71**, 094110.
45 H. Funke, M. Chukalina and A. C. Scheinost, *J. Synchrotron Radiat.*, 2007, **14**, 426–432.
46 G. Chen, M. Ding, K. Zhang, Z. Shen, Y. Wang, J. Ma, A. Wang, Y. Li and H. Xu, *ChemSusChem*, 2022, **15**, e202102352.
47 J. Chen, Y. Kang, W. Zhang, Z. Zhang, Y. Chen, Y. Yang, L. Duan, Y. Li and W. Li, *Angew Chem. Int. Ed. Engl.*, 2022, **61**, e202203022.
48 Y. Gu, B. Xi, W. Tian, H. Zhang, Q. Fu and S. Xiong, *Adv. Mater.*, 2021, **33**, e2100429.
49 L. Han, Z. Ren, P. Ou, H. Cheng, N. Rui, L. Lin, X. Liu, L. Zhuo, J. Song, J. Sun, J. Luo and H. L. Xin, *Angew Chem. Int. Ed. Engl.*, 2021, **60**, 345–350.
50 B. Yu, H. Li, J. White, S. Donne, J. Yi, S. Xi, Y. Fu, G. Henkelman, H. Yu, Z. Chen and T. Ma, *Adv. Funct. Mater.*, 2019, **30**, 1905665.
51 L. Zhang, G. Fan, W. Xu, M. Yu, L. Wang, Z. Yan and F. Cheng, *Chem. Commun.*, 2020, **56**, 11957–11960.
52 Y. Zhao, S. Zhang, C. Han, Q. Lu, Q. Fu, H. Jiang, L. Yang, Y. Xing, Q. Zheng, J. Shen, L. Yan and X. Zhao, *Chem. Eng. J.*, 2023, **468**, 143517.
53 H. Zou, W. Rong, S. Wei, Y. Ji and L. Duan, *Proc. Natl. Acad. Sci. U. S. A.*, 2020, **117**, 29462–29468.